Microfluidics and Nanofluidics (2018) 22:59
https://doi.org/10.1007/s10404-018-2078-9

RESEARCH PAPER

Deterministic lateral displacement (DLD) in the high Reynolds number regime: high-throughput and dynamic separation characteristics

Brian M. Dincau[1] · Arian Aghilinejad[1] · Taylor Hammersley[1] · Xiaolin Chen[1] · Jong-Hoon Kim[1]

Received: 9 February 2018 / Accepted: 12 May 2018 / Published online: 18 May 2018
© Springer-Verlag GmbH Germany, part of Springer Nature 2018

Abstract

Recent progress in the development of biosensors has created a demand for high-throughput sample preparation techniques that can be easily integrated into microfluidic or lab-on-a-chip platforms. One mechanism that may satisfy this demand is deterministic lateral displacement (DLD), which uses hydrodynamic forces to separate particles based on size. Numerous medically relevant cellular organisms, such as circulating tumor cells (10–15 μm) and red blood cells (6–8 μm), can be manipulated using microscale DLD devices. In general, these often-viscous samples require some form of dilution or other treatment prior to microfluidic transport, further increasing the need for high-throughput operation to compensate for the increased sample volume. However, high-throughput DLD devices will require a high flow rate, leading to an increase in Reynolds numbers (*Re*) much higher than those covered by existing studies for microscale (≤ 100 μm) DLD devices. This study characterizes the separation performance for microscale DLD devices in the high-Re regime ($10 < Re < 60$) through numerical simulation and experimental validation. As *Re* increases, streamlines evolve and microvortices emerge in the wake of the pillars, resulting in a particle trajectory shift within the DLD array. This differs from previous DLD works, in that traditional models only account for streamlines that are characteristic of low-*Re* flow, with no consideration for the transformation of these streamlines with increasing *Re*. We have established a trend through numerical modeling, which agrees with our experimental findings, to serve as a guideline for microscale DLD performance in the high-*Re* regime. Finally, this new phenomenon could be exploited to design passive DLD devices with a dynamic separation range, controlled simply by adjusting the device flow rate.

Keywords Separation and purification · High throughput · Deterministic lateral displacement · High Reynolds · Dynamic separation

1 Introduction

Separation and purification of specific targets in a given sample are critical for biosensing applications. This can be challenging, due to the variable nature of most biological samples—often containing a combination of mobile ions, large and small biomolecules, and different cells ranging several orders of magnitude in size (Srinivasan and Tung 2015). Various methodologies have been demonstrated to achieve this goal. Ultrafiltration can be used for isolating species of known size or molecular weight from a sample, but is limited in throughput and requires a secondary "release" step once the sample has been processed (Jungbauer 2013). Microcentrifugation is often employed as a common purification technique, but it is complicated, time-consuming, labor-intensive, and limited in terms of throughput (Dincau et al. 2017b). Ideally, separation and purification techniques should be rapid and simple, such that they may be easily incorporated over a wide range of sensing applications.

Microfluidic devices have shown a significant potential to enhance our biosensing and processing capabilities due to their precise control, rapid process times, and ease of automation (Gilmore et al. 2016; Hou et al. 2011; Warkiani et al. 2015). In fact, there has already been a surge in microfluidic purification platforms that utilize magnetism and/or electrokinetics

Electronic supplementary material The online version of this article (https://doi.org/10.1007/s10404-018-2078-9) contains supplementary material, which is available to authorized users.

✉ Jong-Hoon Kim
jh.kim@wsu.edu

[1] School of Engineering and Computer Science, Washington State University, Vancouver, WA 98686, USA

(Aghilinejad et al. 2018) to concentrate bioparticles significantly faster than the conventional filtration and centrifugation technologies (Dincau et al. 2017b). One drawback of these early devices is their reliance on additional sample modification to facilitate purification, such as conjugation with engineered nanoparticles. Another drawback is their inability to handle larger sample volumes (mL–L), which ultimately limits sensitivity. A larger sample volume will contain greater levels of a target analyte—be it DNA, viral particles, or another bio indicator—thereby increasing the chances of a successful assay. Thus, there is a growing demand for simple, direct purification platforms that can handle larger sample volumes without sacrificing any of the other advantages that microfluidics offer.

Analytes that behave as particles, such as cells, viruses, and large macromolecules, can be effectively isolated through selective mechanical separation. One such microfluidic device that is capable of passive, continuous, size-based particle separation is a deterministic lateral displacement (DLD) device, originally demonstrated in 2004 (Huang et al. 2004). These devices use an array of micro pillars to influence particle displacement according to hydrodynamic forces that emerge under flow conditions. Particles with mean diameters greater than the critical diameter (D_c) are displaced laterally as they pass through the array, while smaller particles undergo significantly less lateral displacement. This D_c has been approximated as both a linear (Inglis et al. 2006) and power function (Davis 2008), dependent only on the device geometry:

$$D_c \approx 2\alpha G \left({}^{\Delta}/_{\lambda} \right). \tag{1}$$

$$D_c \approx 1.4G \left({}^{\Delta}/_{\lambda} \right)^{0.48}, \tag{2}$$

where G is the vertical gap size between pillars, Δ is the row shift, λ is the period of the array, and α is a dimensionless correction factor. Since DLD separation is both continuous and mechanically deterministic, these devices could be easily incorporated as in-line sample purification units within greater biosensing systems.

Like most microfluidics, DLD devices have traditionally operated in the laminar regime, with Reynolds numbers less than 1. As shown in Fig. 1a, this allows for predictable streamline formation and consistent particle movement; the critical diameter follows the approximate relationships stated above in Eqs. (1) and (2). This means that multiple distinct arrays are required for the fractionation of samples containing more than two analytes. As a result, there have been many attempts to manipulate and enhance the separation characteristics of DLD arrays, including the utilization of asymmetric gap sizes (Zeming et al. 2016a), different geometric pillar shapes (Zhang et al. 2015), additional external forces [dielectrophoretic (Beech et al. 2009), gravitational (Devendra and Drazer 2012), centrifugal (Jiang et al. 2016)], and various buffer additives such as sodium chloride (NaCl) (Zeming et al. 2016b) and polyethylene glycol (PEG) (Chen et al. 2015). Still, each of these groups has focused on performance in the low-*Re* regime with relatively low fluid velocities. These low velocities restrict throughput, often reported in the mL/h or μL/min range, which has limited the sample volumes that these devices are capable of processing.

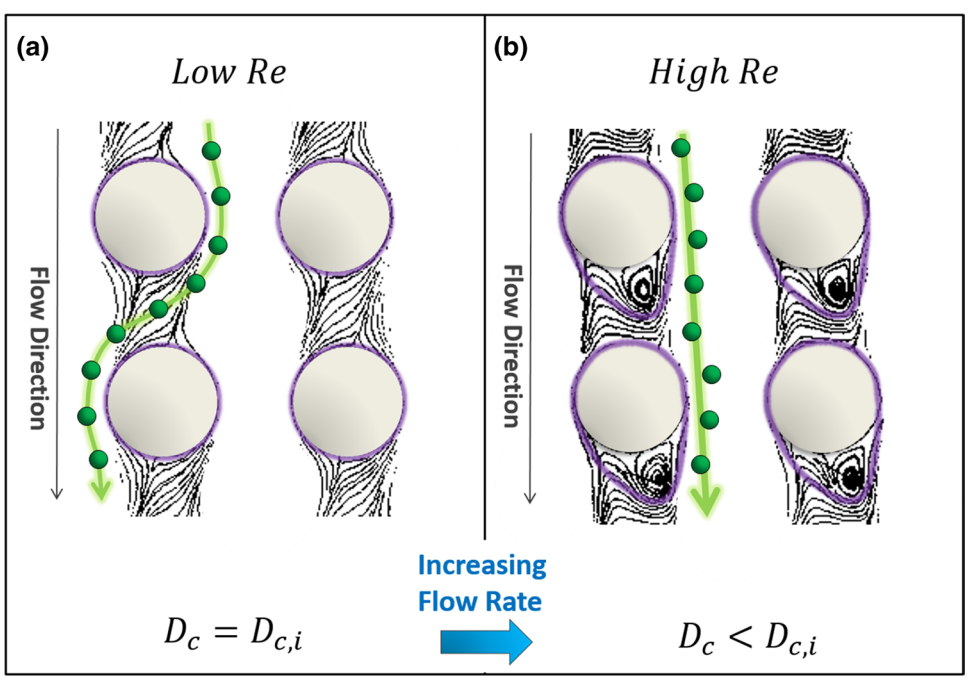

Fig. 1 Illustration depicting high-*Re*-induced shift in D_c, with particle trajectories in green and effective hydrodynamic pillar geometry outlined in purple. **a** Particles smaller than the baseline D_c follow a non-displacement mode in low-*Re* regime. **b** Identical particles follow the displacement mode in high-*Re* flow due to vortex effects and streamline disruption increasing the effective hydrodynamic size of pillars

To the best of our knowledge, there have been no comprehensive studies that focus on microscale DLD performance in high Reynolds number regimes, with limited studies at the macroscale (Lubbersen et al. 2013) or in the moderate Reynolds number regime ($Re \leq 18$) (Lubbersen et al. 2012).

In this study, we investigate DLD performance in the high-*Re* regime for high-throughput and high-volume functionality. According to general fluid mechanics, inertial forces become more significant with increasing *Re*, resulting in altered streamlines and microvortex development in the wake of the pillars at a sufficiently high flow rate (Dincau et al. 2017a). These vortices may increase the apparent hydrodynamic size of the pillars, consequently reducing the effective gap length and resulting in a dynamic shift in D_c as the flow rate increases, as summarized in Fig. 1b and demonstrated at the macroscale by Lubbersen et al. The relationship between Reynolds number and D_c is investigated by characterizing DLD performance over a range of Reynolds values ($1 < Re < 60$), through both simulation and experimental study with a high-speed camera. Based on numerical results, this range was chosen, because it describes the complete transition from smooth laminar flow to well-developed microvortices, with gradually shifting streamlines throughout. Finally, with these results, we aim to provide some additional design considerations for high-throughput DLD devices operating in the high-*Re* regime.

2 Materials and methods

2.1 Numerical simulation parameters

To evaluate the effects of increasing *Re* on DLD performance, two-dimensional geometries with circular-shaped posts were implemented in COMSOL Multiphysics (Comsol, Inc. Palo Alto, CA), a finite-element-based software package. The DLD arrays were modeled with pillar and gap dimensions identical to those of the experimental devices. A constant flow velocity was applied at the inlet, and the outlet was fixed at atmospheric pressure with no-slip conditions employed for all the other boundaries. The simulations were carried out over a wide range of inlet fluid velocities, corresponding to $0.1 < Re < 75$, and the fluid was assumed to be incompressible with the properties of water: density $\rho = 1000$ kg/m^3 and viscosity $\eta = 0.001$ kg/m s. The Navier–Stokes and continuity equations were solved for obtaining the flow field. Then, utilizing the velocity data from fluid flow and employing a particle tracing model, the particle trajectories were investigated inside the microchannel. These injected particles were used to visualize the fluid flow direction and the effect of inlet velocity on separation behavior. With the expectation that D_c will vary with flow rate, we henceforth refer to the initial low-*Re* critical diameter as $D_{c,i}$ while D_c represents the critical diameter at a given flow rate or Reynolds number.

2.2 Device fabrication

All experimental devices were fabricated using conventional soft lithography. Negative features were photolithographically patterned using SU-8 2100 series photoresist (Microchem Corp. Westborough, MA) on a 4 in. silicon substrate. Fabrication specifics, such as spin speeds and bake parameters, are outlined in Table 1. Development was performed in an ultrasonic bath to accelerate the development of via hole features. Finally, the wafer was hard-baked to ensure thermal stability of the mold throughout the casting process. Once hard-baked, the SU-8 mold was complete and could be re-used several times to generate a sufficient number of devices. It should be noted that thick SU-8 features are highly susceptible to thermally induced cracking and delamination from the silicon substrate. This effect was mitigated by creating a thin base layer of exposed SU-8 to serve as the effective substrate surface (Henry et al. 2015), as well as ensuring a slow temperature ramp during all heating and cooling steps. Additional steps were also taken to minimize edge bead thickness (Lee et al. 2011), which can negatively impact photolithography resolution if left unmitigated.

Before PDMS (Polydimethylsiloxane, SYLGARD® 184, Dow Corning Corp.) casting, the mold should be thoroughly silanized in order to facilitate a clean release process. This was done by incubating a 15 µL droplet of trichlorosilane (Sigma-Aldrich) with the mold and casting container in a low-pressure desiccator overnight. Prepared PDMS was then poured over the mold features and cured in an oven at 95 °C. The devices were then removed from the mold, cut to shape and cleaned, and then bonded to a glass slide by oxygen plasma treatment. This procedure was used to fabricate two device configurations, with representative relevant dimensions as summarized in Fig. 2.

2.3 Experimental setup and analysis methods

The primary goal of the experimental portion of this investigation was to characterize DLD separation performance over a range of moderate- to high-*Re* flow rates. Each

Table 1 Fabrication parameters for SU-8 molds

Device Number	1	2
Spin speed	1300 rpm	2000 rpm
Soft bake temp	65 °C/95 °C	65 °C/95 °C
Soft bake time	15 min./50 min.	10 min./45 min.
PEB temp	65 °C/95 °C	65 °C/75 °C
PEB time	10 min./15 min.	5 min./30 min.

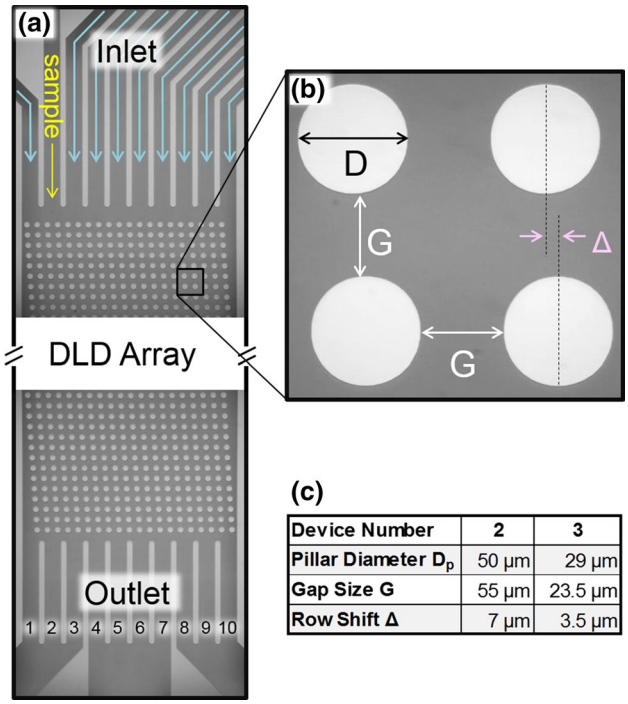

(c)

Device Number	2	3
Pillar Diameter D_p	50 μm	29 μm
Gap Size G	55 μm	23.5 μm
Row Shift Δ	7 μm	3.5 μm

Fig. 2 Comprehensive summary of device configuration and relevant parameters. **a** Micrograph of a representative photomask used for device fabrication. Buffer pathways are shown in light blue, while the sample injection is shown in yellow. Outlet channels are numbered sequentially from left to right. **b** Close-up of the DLD array with relevant dimensions depicted. **c** Concise table of dimensional values for Device 1 and Device 2

experimental trial consisted of setting the desired flow rate with an array of syringe pumps (kdScientific KDS-200, New Era NE-1000X), taking care to wait for the system to reach equilibrium, then slowly injecting a polystyrene microparticle suspension (Thermo Scientific, Sigma-Aldrich, Phosphorex, Max Std Dev < 2% of the nominal particle size) through the sample inlet. The detailed experimental setup is shown in supplementary info (Fig. S1). The inlet configuration can be seen in Fig. 2a with relevant device dimensions outlined in Fig. 2b, c. Deionized water was chosen as the buffer and working fluid for this study. After particle injection, dynamic separation performance was recorded at the device outlet using a high-speed camera (Phantom Mira 310) mounted atop an optical microscope (Nikon Eclipse Ci). Typical recordings were captured at 8000–12,000 frames per second to ensure frame-to-frame particle traceability. Particle velocities were obtained using the phantom camera control (PCC) application, wherein individual particles were manually traced from frame-to-frame (see supplementary info). The distance traveled was determined using known device dimensions as a reference, while the frame time was recorded during capture. Particle distributions were also obtained using PCC, wherein an average normalized distribution was determined by manual counting of particles across 20 independent frames (frames that share no common particles). Particle distributions at the outlet were used to observe and quantify any shift in D_c from trial-to-trial as the flow rates were varied.

3 Discussion of results

3.1 Numerical results

The first step in this numerical investigation aimed at determining which *Re* values microvortices would begin to develop within a DLD array, as illustrated by the representative flow fields shown in Fig. 3. When $Re = 0.1$, the flow is smooth and continuous (Fig. 3a). This is the characteristic flow regime for the majority of previously studied DLD devices. Vortices begin to emerge around $Re = 25$ (Fig. 3b), but do not fully develop until $Re = 50$ (Fig. 3c). At this point, the microvortices are nearly half the size of the pillars and significantly alter the streamlines as they traverse the crossover region between pillars. The vortices do not continue to grow significantly beyond this point, as demonstrated by a similar size and shape at $Re = 75$ (Fig. 3d). Based on this information, it was determined that $25 < Re < 75$ is a reasonable range to consider "high-*Re*" for the purpose of this study.

Figure 4 shows the simulation results for particle tracing to compare the trajectories in high- and low-*Re* flows with modeled flow fields. For this investigation, we present the particle size (d_p) as a ratio of the initial critical diameter ($D_{c,i}$), such that $d_p/D_{c,i} = 0.8$. Thus, the particle is 20% smaller than the initial critical diameter for this array configuration. At low-*Re* values, the particle follows a zigzag mode that yields no net displacement (Fig. 4a). This is expected and agrees with the previous DLD works. However, at $Re = 25$, the same particle now follows a bumped mode that yields a significant lateral displacement (Fig. 4b). This differs from previous DLD works; in that, this particle would traditionally have been assumed to follow the same zig-zag mode, because traditional DLD modeling has assumed laminar flow with continuous and orderly streamlines. By evaluating streamline evolution and vortex effects in this analysis, it is clear that the traditional models for approximating D_c are insufficient for high-*Re* flows.

3.2 Experimental results

Results from the experimental trials are summarized in Fig. 5. Each entry consists of a composite image at the device outlet, which overlays several independent high-speed frames to emphasize the visible trajectory. Below each

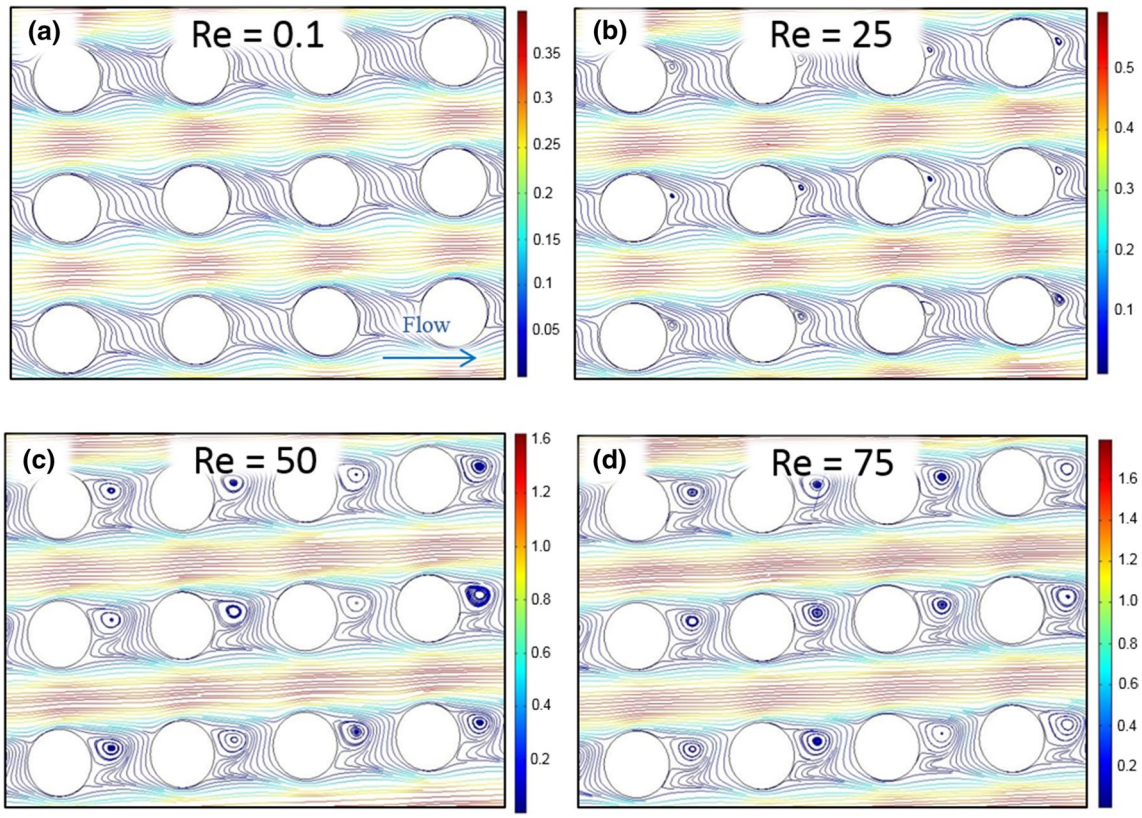

Fig. 3 Simulated velocity fields within a DLD array with increasing Reynolds numbers. Pillar diameter and gap size dimensions correspond to those of Device 1. Velocity scales to the right of each window are all in m/s. **a** At $Re = 0.1$, the flow is characteristically laminar with no apparent vortices or separation. **b** At $Re = 25$, vortices begin to appear in the wake of the pillars. **c** At $Re = 50$, the vortices have grown significantly with little change in appearance at higher flow rates, as illustrated in **d** at $Re = 75$

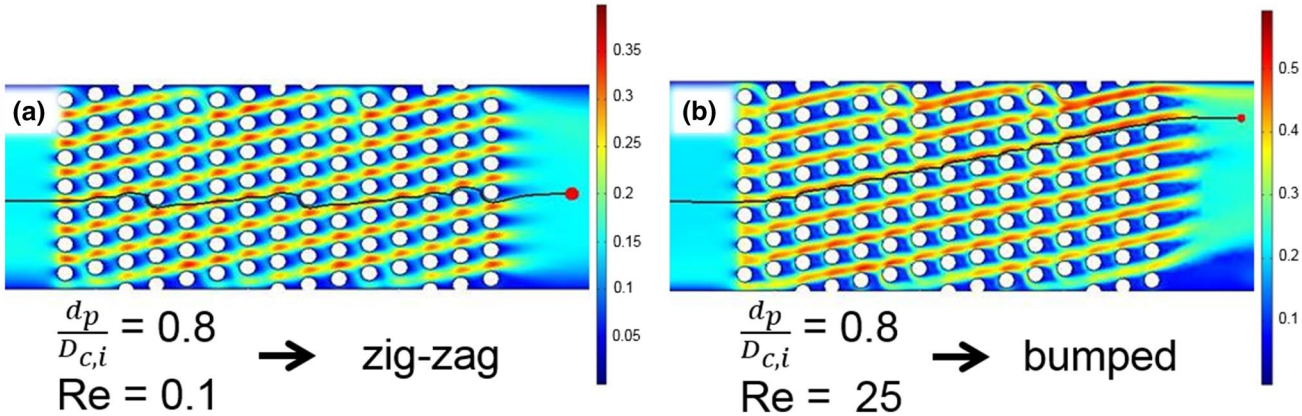

Fig. 4 Simulation results for the trajectories of identical particles ($d_p/D_{c,i} = 0.8$) in two different flow regimes. Velocity scales are in m/s. **a** At $Re = 0.1$, the particle follows a zig-zag mode, yielding no net displacement. **b** At $Re = 25$, the same particle follows a bumped mode, resulting in lateral displacement

image is a corresponding normalized particle distribution to quantify that trajectory.

Device 1 was characterized using three different particle sizes (10, 15, and 20 μm) across a range of flow rates corresponding to *Re* values from 8 to 58. Over this range, there is a clear shift in operating D_c as the Reynolds number climbs. This is demonstrated by the change in particle distribution at the device outlet, shifting from left (zig-zag

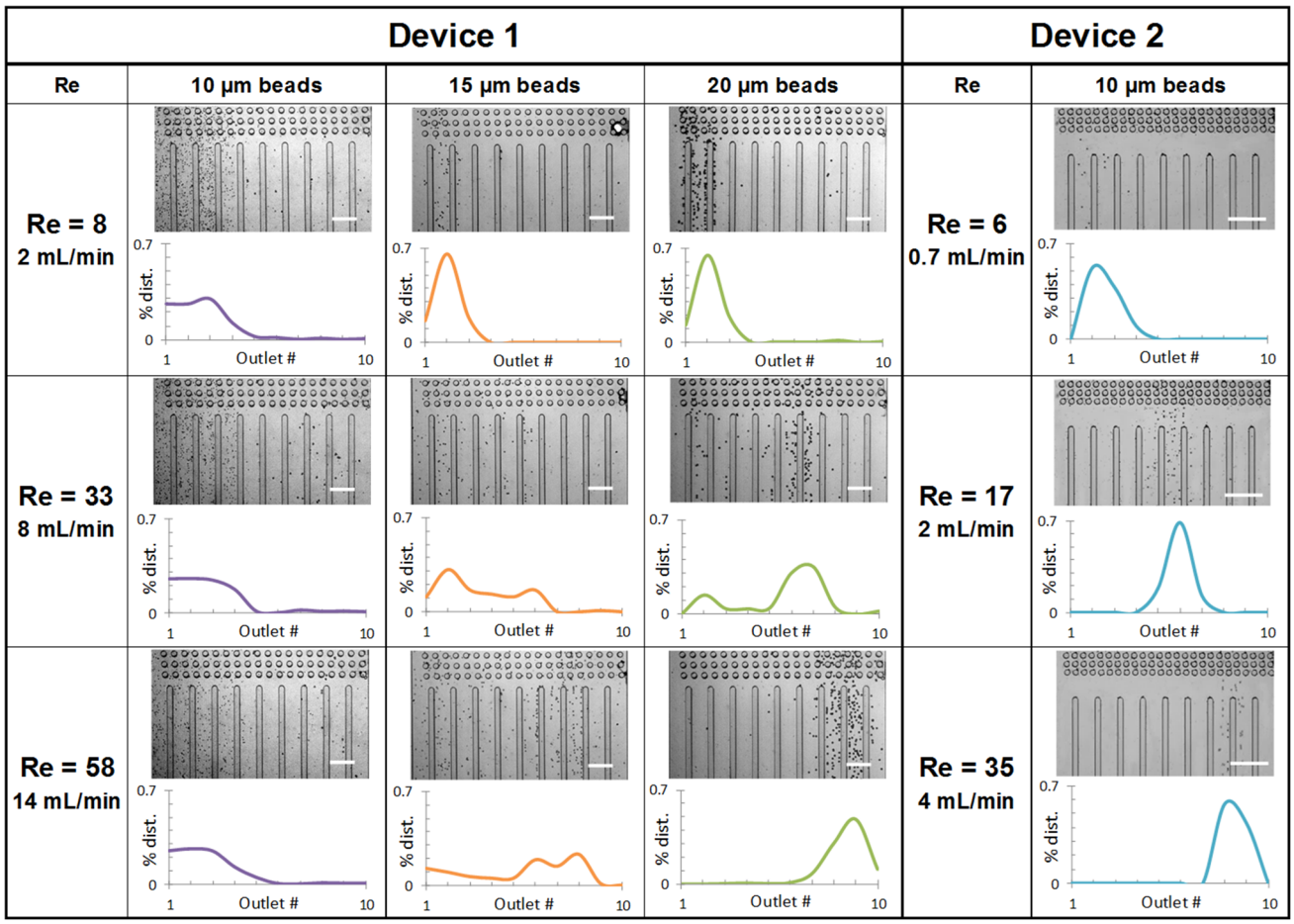

Fig. 5 Summary of experimental results, which demonstrate a shift in particle trajectories with increasing flow rates. For each entry, a composite micrograph of the device outlet illustrates bulk particle trajectories, with 250 µm scale bar shown in white. Below each micrograph is the normalized particle distribution, whose *x*-axis represents outlet channel number (left-most = 1 ; right-most = 10), and *y*-axis represents the corresponding percentage of particles. For both devices, there is a clear shift in operating D_c with increasing flowrate, as indicated by the shifting particle distribution at the outlet. The transition from left to right represents a particle's transition from a zig-zag mode to a bumped mode

mode) to right (bumped mode) as the flow rate increases. All particles follow the zig-zag mode at $Re = 8$, thus would all be considered smaller than the current device D_c. Their behavior diverges with increasing *Re*, however, depending on the particle size. The 20 µm particles show a drastic shift in their outlet distribution, whose peak moves from outlet channel 2 to channel 7 when $Re = 33$, migrating even further to channel 9 at $Re = 58$. Note that this corresponds to a flow rate of 14 mL/min, which is several orders of magnitude faster than similar conventional DLD arrays having $D_c \approx 20$ µm (McGrath et al. 2014), and 40% faster than the optimized mirrored array demonstrated by Loutherback et al. (2012). We believe that this throughput could still be significantly increased through further optimization. Similarly, the 15 µm particles also show a clear, but less drastic shift. The 10 µm particles show no shift in their outlet distribution, which thus remained below D_c over the entire *Re* range.

Device 2, which served to support the initial findings from Device 1, was characterized using only 10 µm particles across a range of flow rates corresponding to *Re* values from 6 to 35. Higher *Re* values could not be reliably investigated, due to pressure limitations in the experimental system. For Device 2, the same trend was observed. While the 10 µm particles follow a zig-zag mode at $Re = 6$, their trajectory shifts to the bumped mode with increasing *Re*. It appears that Device 2 experienced the D_c shift at a lower *Re* than Device 1, even before we predict vortices to emerge at $Re = 25$. This indicates that the shift may not be purely a result of vortex development, but a combined effect that also includes streamline evolution with increasing *Re*. This is further substantiated in Fig. 6, which combines the experimental results with our numerical model. It should also be noted that, in several cases, secondary distribution peaks are observed for particles of the same size during the transition

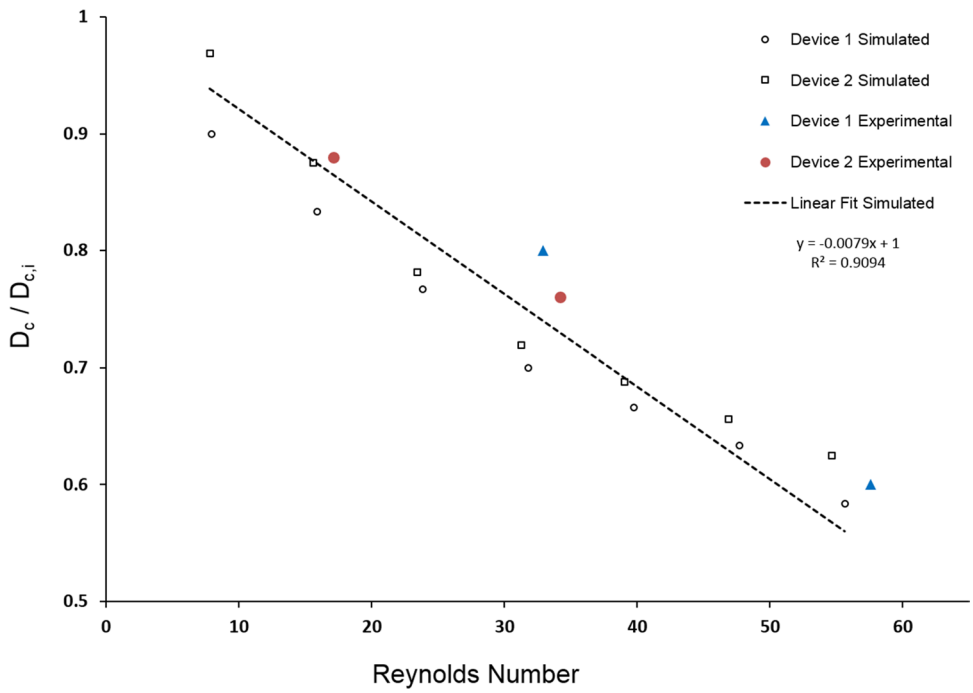

Fig. 6 Simulated scaling analysis for both devices, showing decreasing $D_c/D_{c,i}$ (thus decreasing D_c) with increasing Reynolds number. Theoretical data points were obtained through iterative simulation. Experimental data points—approximated based on device performance at varying flow rates—are plotted as well, demonstrating a strong correlation between the simulated and observed D_c shift. The dashed line represents a combined linear fit for both simulated data sets

from a zig-zag to bumped mode. While the exact nature of these secondary peaks is not yet fully understood, they indicate some degree of flow instability or asymmetry with increasing *Re*. The influence of growing microvortices may have a chaotic effect on particle trajectories. In addition, it has been shown that an asymmetric flow profile develops between pillars in high-*Re* flow, and thus, some particles may experience slightly different velocities as they pass through the device, resulting in a less-pronounced secondary trajectory. This effect appears to be reduced for smaller particles, as the 10 µm particles did not exhibit this multi-mode path in either device.

These results clearly indicate a relationship between D_c and *Re*, the effects of which become quite drastic as flow rates increase, even with *Re* values as low as 17. This means that increasing *Re* can alter device functionality simply by altering streamlines, even before microvortices emerge. This is important to consider for any high-throughput DLD design scenario, in which higher flow rates will result in higher *Re* values. In addition, this new phenomenon could be utilized in designing passive DLD devices having a dynamic D_c with micrometer resolution. For the continuous separation and isolation of various types of cells in a sample (e.g., human cells), it has the advantages of (1) handling large volume samples with a continuous stream of dispersed particles and (2) dynamically tuning the separation range with an excellent size resolution.

The experimental results verify the trend established by our numerical model, in which D_c and $D_{c,i}$ can be more precisely approximated by defining exact particle sizes. With future DLD design in mind, we have plotted several numerical and experimental findings in Fig. 6 to provide some basic reference. In this graph, we have non-dimensionalized the shift in D_c by plotting it as a ratio over $D_{c,i}$. This allows for the comparison of both devices, despite operating at different scales. Notice that both theoretical data sets follow a nearly identical decreasing trend. Similarly, while there is some degree of deviation, the experimental data points show a strong correlation with the theoretical data. While the exact relationship is still not fully understood, we have chosen a linear fit based on the approximate shape of the data and a reasonable R^2 value of 0.91. Therefore, this plot may serve as an effective model in predicting DLD separation performance at high-*Re* values when coupled with the traditional approximations for $D_{c,i}$. Note that the usefulness of this data set is inherently dependent on the Reynolds number calculation. For this investigation, the characteristic length was defined as the gap size between pillars (G in Fig. 2c), while the characteristic velocity is the average fluid velocity between pillars. The relationship between flow rate and velocity in experimental devices is shown in supplementary info (Fig. S2).

4 Conclusion

We have presented and demonstrated a relatively simple microfluidic-based scheme capable of sorting particles with high throughput (up to 14 mL/min) and excellent size resolution. There is a growing demand for high-throughput sample preparation techniques to support the next generation of microfluidics-based biosensors. In the case of DLD devices,

this will require higher flow rates resulting in flow regimes with significantly higher Reynolds numbers than previously investigated. Therefore, the separation performance for a set of microscale DLD devices has been characterized over the range of $10 < Re < 60$. Through numerical investigation and experimental validation, this study has shown that separation performance can vary with micrometer resolution as Re increases. This is due to streamline transformation and the emergence of microvortices in the wake of the pillars under high-velocity flow conditions. The result of this is a shift in D_c, which decreases with increasing Re. This phenomenon should be accounted for in high-throughput DLD design; otherwise, the resulting device will not separate particles of the desired size. To facilitate this consideration, we have presented a plot indicating the general relationship between $D_c/D_{c,i}$ and Re. This trend could be used to better estimate D_c for a given Re, as demonstrated by the plotted experimental data. In addition, this phenomenon could be utilized in designing passive DLD devices with a dynamic D_c, wherein the separation performance can be tuned by simply adjusting the flow rate.

Acknowledgements J.-H.K. acknowledges funding for this work provided by the New Faculty Seed Grant (131078) from Washington State University.

Compliance with ethical standards

Conflict of interest The authors declare that they have no conflict of interest.

References

Aghilinejad A, Aghaamoo M, Chen XL, Xu J (2018) Effects of electrothermal vortices on insulator-based dielectrophoresis for circulating tumor cell separation. Electrophoresis 39:869–877. https://doi.org/10.1002/elps.201700264

Beech JP, Jonsson P, Tegenfeldt JO (2009) Tipping the balance of deterministic lateral displacement devices using dielectrophoresis. Lab Chip 9:2698–2706. https://doi.org/10.1039/b823275j

Chen Y, Abrams ES, Boles TC, Pedersen JN, Flyvbjerg H, Austin RH, Sturm JC (2015) Concentrating genomic length DNA in a microfabricated array. Phys Rev Lett. https://doi.org/10.1103/PhysRevLett.114.198303

Davis JA (2008) Microfluidic separation of blood components through deterministic lateral displacement. Princeton University, Princeton

Devendra R, Drazer G (2012) Gravity driven deterministic lateral displacement for particle separation in microfluidic devices. Anal Chem 84:10621–10627. https://doi.org/10.1021/ac302074b

Dincau B, Aghilinejad A, Kim J-H, Chen X (2017a) Characterizing the high reynolds number regime for deterministic lateral displacement (DLD) devices. Paper presented at the ASME international mechanical engineering congress and exposition, Tampa, FL

Dincau BM, Lee Y, Kim JH, Yeo WH (2017b) Recent advances in nanoparticle concentration and their application in viral detection using integrated sensors. Sensors. https://doi.org/10.3390/s17102316

Gilmore J, Islam M, Martinez-Duarte R (2016) Challenges in the use of compact disc-based centrifugal microfluidics for healthcare diagnostics at the extreme point of care. Micromachines. https://doi.org/10.3390/mi7040052

Henry S, Johnson E, Wen J (2015) SU-8 Delamination Resistance Study Report, 24 February, 2015 edn. University of Pennsylvania Scholarly Commons

Hou HW, Bhagat AAS, Lee WC, Huang S, Han J, Lim CT (2011) Microfluidic devices for blood fractionation. Micromachines 2:319–343. https://doi.org/10.3390/mi2030319

Huang LR, Cox EC, Austin RH, Sturm JC (2004) Continuous particle separation through deterministic lateral displacement. Science 304:987–990. https://doi.org/10.1126/science.1094567

Inglis DW, Davis JA, Austin RH, Sturm JC (2006) Critical particle size for fractionation by deterministic lateral displacement. Lab Chip 6:655–658. https://doi.org/10.1039/b515371a

Jiang ML, Mazzeo AD, Drazer G (2016) Centrifuge-based deterministic lateral displacement separation. Microfluid Nanofluid 20:10. https://doi.org/10.1007/s10404-015-1686-x

Jungbauer A (2013) Continuous downstream processing of biopharmaceuticals. Trends Biotechnol 31:479–492. https://doi.org/10.1016/j.tibtech.2013.05.011

Lee H, Lee K, Ahn B, Xu J, Xu LF, Woh K (2011) A new fabrication process for uniform SU-8 thick photoresist structures by simultaneously removing edge bead and air bubbles J Micromech Microeng. https://doi.org/10.1088/0960-1317/21/12/125006

Loutherback K, D'Silva J, Liu LY, Wu A, Austin RH, Sturm JC (2012) Deterministic separation of cancer cells from blood at 10 mL/min. Aip Adv. https://doi.org/10.1063/1.4758131

Lubbersen YS, Schutyser MAI, Boom RM (2012) Suspension separation with deterministic ratchets at moderate Reynolds numbers. Chem Eng Sci 73:314–320. https://doi.org/10.1016/j.ces.2012.02.002

Lubbersen YS, Dijkshoorn JP, Schutyser MAI, Boom RM (2013) Visualization of inertial flow in deterministic ratchets. Sep Purif Technol 109:33–39. https://doi.org/10.1016/j.seppur.2013.02.028

McGrath J, Jimenez M, Bridle H (2014) Deterministic lateral displacement for particle separation: a review. Lab Chip 14:4139–4158. https://doi.org/10.1039/c4lc00939h

Srinivasan B, Tung S (2015) Development and applications of portable biosensors. Jala 20:365–389. https://doi.org/10.1177/2211068215581349

Warkiani ME, Wu LD, Tay AKP, Han J (2015) Large-volume microfluidic cell sorting for biomedical applications. In: Yarmush ML (ed) Annual review of biomedical engineering, vol 17, pp 1–34. https://doi.org/10.1146/annurev-bioeng-071114-040818

Zeming KK, Salafi T, Chen CH, Zhang Y (2016a) Asymmetrical deterministic lateral displacement gaps for dual functions of enhanced separation and throughput of red blood cells. Sci Rep. https://doi.org/10.1038/srep22934

Zeming KK, Thakor NV, Zhang Y, Chen CH (2016b) Real-time modulated nanoparticle separation with an ultra-large dynamic range. Lab Chip 16:75–85. https://doi.org/10.1039/c5lc01051a

Zhang ZM, Henry E, Gompper G, Fedosov DA (2015) Behavior of rigid and deformable particles in deterministic lateral displacement devices with different post shapes. J Chem Phys. https://doi.org/10.1063/1.4937171

Publisher's Note Springer Nature remains neutral with regard to jurisdictional claims in published maps and institutional affiliations.